ARTICLES
https://doi.org/10.1038/s41551-020-00638-0

nature biomedical engineering

A portable single-sided magnetic-resonance sensor for the grading of liver steatosis and fibrosis

Ashvin Bashyam[1,2,9], Chris J. Frangieh[1,2,9], Siavash Raigani[3], Jeremy Sogo[1,2], Roderick T. Bronson[4], Korkut Uygun[5], Heidi Yeh[3], Dennis A. Ausiello[6,7] and Michael J. Cima[1,8] ✉

Low-cost non-invasive diagnostic tools for staging the progression of non-alcoholic chronic liver failure from fatty liver disease to steatohepatitis are unavailable. Here, we describe the development and performance of a portable single-sided magnetic-resonance sensor for grading liver steatosis and fibrosis using diffusion-weighted multicomponent T2 relaxometry. In a diet-induced mouse model of non-alcoholic fatty liver disease, the sensor achieved overall accuracies of 92% (Cohen's kappa, $\kappa = 0.89$) and 86% ($\kappa = 0.78$) in the ex vivo grading of steatosis and fibrosis, respectively. Localization of the measurements in living mice through frequency-dependent spatial encoding led to an overall accuracy of 87% ($\kappa = 0.81$) for the grading of steatosis. In human liver samples, the sensor graded steatosis with an overall accuracy of 93% ($\kappa = 0.88$). The use of T2 relaxometry as a sensitive measure in fully automated low-cost magnetic-resonance devices at the point of care would alleviate the accessibility and cost limits of magnetic-resonance imaging for diagnosing liver disease and assessing liver health before liver transplantation.

Non-alcoholic fatty liver disease (NAFLD) and non-alcoholic steatohepatitis (NASH) together are the leading cause of chronic liver disease in the United States and affect more than 1 billion adults worldwide[1,2]. It is estimated that 30–40% of US adults have NAFLD, and approximately 20% of the cases are expected to progress to NASH[3]. NAFLD is characterized by abnormal fat accumulation (steatosis) in the liver and, when it progresses to NASH, is defined by inflammation and varying degrees of fibrosis[4]. There is no widely available non-invasive diagnostic that can distinguish between patients with NAFLD and NASH. Such a measurement may enable earlier intervention, such as diet or lifestyle modifications, bariatric surgery and pharmacologic therapies (for example, pioglitazone and liraglutide) to prevent the progression from simple steatosis to steatohepatitis and, eventually, cirrhosis and hepatocellular carcinoma. These patients are also at higher risk of developing end-stage liver disease, for which the only cure is liver transplantation[5,6]. Thus, direct measurement of steatosis and fibrosis may provide a highly robust diagnosis as there is a clinical need for improved diagnostic and prognostic technologies for NAFLD and NASH.

New approaches would enable more proactive screening of at-risk individuals before clinical symptoms become apparent, longitudinal tracking of disease progression to guide clinical interventions and serve as a surrogate marker to support the clinical development of new therapeutics[7–9]. The ideal technology would be non-invasive, low-cost, sensitive and specific while offering both straightforward operation and an easily interpretable report[1,9,10]. Existing approaches have the following limitations: liver biopsy is highly invasive and suffers from sampling bias; ultrasound suffers from high interoperator variability and limited specificity; and serum markers are not specific to NAFLD and NASH and are sensitive only to severe disease[11–14]. Magnetic-resonance elastography (MRE) has shown promise in grading fibrosis in the clinical setting, but its high cost, driven by the need for specialized hardware, may limit its widespread access, similar to magnetic-resonance imaging (MRI)[15,16].

Magnetic resonance (MR) is exquisitely sensitive to changes in tissue architecture and composition induced by liver steatosis and fibrosis[17–19]. A quantitative MRI scan has the ability to robustly extract clinically meaningful steatosis and fibrosis grades using multicomponent T2 relaxometry across a heterogeneous patient population with varied physiology and disease states[20,21]. However, its high cost, the large number of patients that need to be screened, its requirement for a skilled operator and radiologist, its long acquisition times and its limited accessibility preclude MRI as a widely available diagnostic for highly prevalent liver diseases[22–24]. A portable MR sensor for steatosis and fibrosis grading would leverage the diagnostic power of MRI while overcoming many of the shortcomings of both MRI and existing approaches to NASH/NAFLD diagnostics.

Here we demonstrate accurate staging of steatosis and fibrosis in mouse and human livers using a portable MR sensor with histological validation. Our approach leverages diffusion-weighted (DW) multicomponent T2 relaxometry to provide a quantitative predictor

[1]David H. Koch Institute for Integrative Cancer Research, Massachusetts Institute of Technology, Cambridge, MA, USA. [2]Electrical Engineering & Computer Science, Massachusetts Institute of Technology, Cambridge, MA, USA. [3]Division of Transplantation, Department of Surgery, Massachusetts General Hospital, Boston, MA, USA. [4]Department of Microbiology and Immunobiology, Division of Immunology, Harvard Medical School, Boston, MA, USA. [5]Center for Engineering in Medicine and Surgery, Massachusetts General Hospital, Boston, MA, USA. [6]Division of Nephrology, Department of Medicine, Massachusetts General Hospital, Boston, MA, USA. [7]Center for Assessment Technology and Continuous Health, Massachusetts General Hospital, Boston, MA, USA. [8]Department of Materials Science and Engineering, Massachusetts Institute of Technology, Cambridge, MA, USA. [9]These authors contributed equally: Ashvin Bashyam, Chris J. Frangieh. ✉e-mail: mjcima@mit.edu

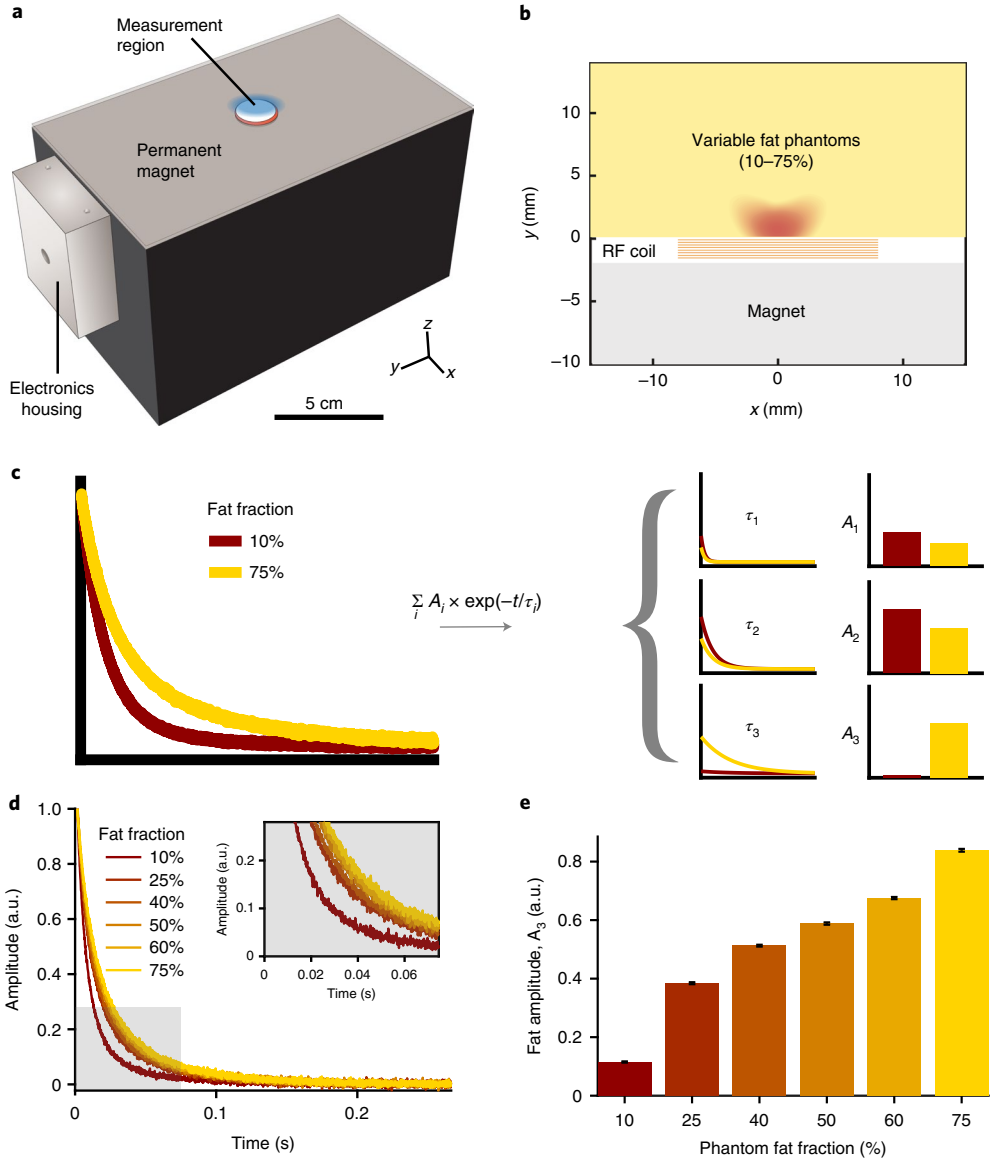

Fig. 1 | A portable MR sensor can accurately quantify fat content. a, An illustration of the prototype portable single-sided MR sensor for preclinical validation studies. **b**, Experimental schematic for quantifying the fat fraction within synthetic tissue phantoms of variable fat content. **c**, Schematic of signal decomposition for the multicomponent T2 relaxometry data analysis technique. A_i and τ_i correspond to the amplitude and relaxation time, respectively, for a particular relaxation component. **d**, Time-domain decay curves acquired using the portable MR sensor for each synthetic tissue phantom. **e**, Fat amplitude extracted from portable MR sensor measurements of synthetic tissue phantoms. The error bars represent the 95% confidence intervals (CIs) of amplitude estimates. a.u., arbitrary units.

of both steatosis and fibrosis. We first demonstrated the ability of the sensor to robustly quantify steatosis grade using synthetic tissue phantoms. We then used the portable MR sensor to stage steatosis and fibrosis, both ex vivo and in vivo, in a mouse model of NAFLD/NASH and, finally, validated this in human liver tissue samples.

Results

The portable MR sensor accurately quantifies the fat fraction in synthetic tissue phantoms. We previously designed and constructed a portable, single-sided MR sensor that has the ability to perform localized MR measurements[25] (Fig. 1a). The sensor contains a magnet assembly, based on the Unilateral Linear Halbach design, and a solenoid radiofrequency (RF) transceiver coil[26] (Supplementary Fig. 1). The magnet assembly produces a remote, uniform static magnetic field that, in combination with the RF transceiver coil, has the ability to perform a measurement distal from the surface of the sensor.

We sought to demonstrate accurate estimation of fat fraction in known samples using the portable MR sensor. We synthesized synthetic tissue phantoms spanning a wide range of fat fractions (10–75% fat) consisting of emulsions of peanut oil and agar hydrogel[27]. Microscopy images of phantoms (Supplementary Fig. 2a,b) confirmed the presence of emulsified oil droplets contained within the hydrogel matrix[28]. These phantoms emulate the range of fat fractions that are observed in healthy and fatty human liver and exhibit MR relaxation properties that are similar to those observed in these tissues[29]. The relaxation times and relative amplitudes of low- and high-fat phantoms show high concordance with those of low and high steatosis mouse livers, respectively (Supplementary Fig. 3). Each phantom was measured with the portable MR sensor using a

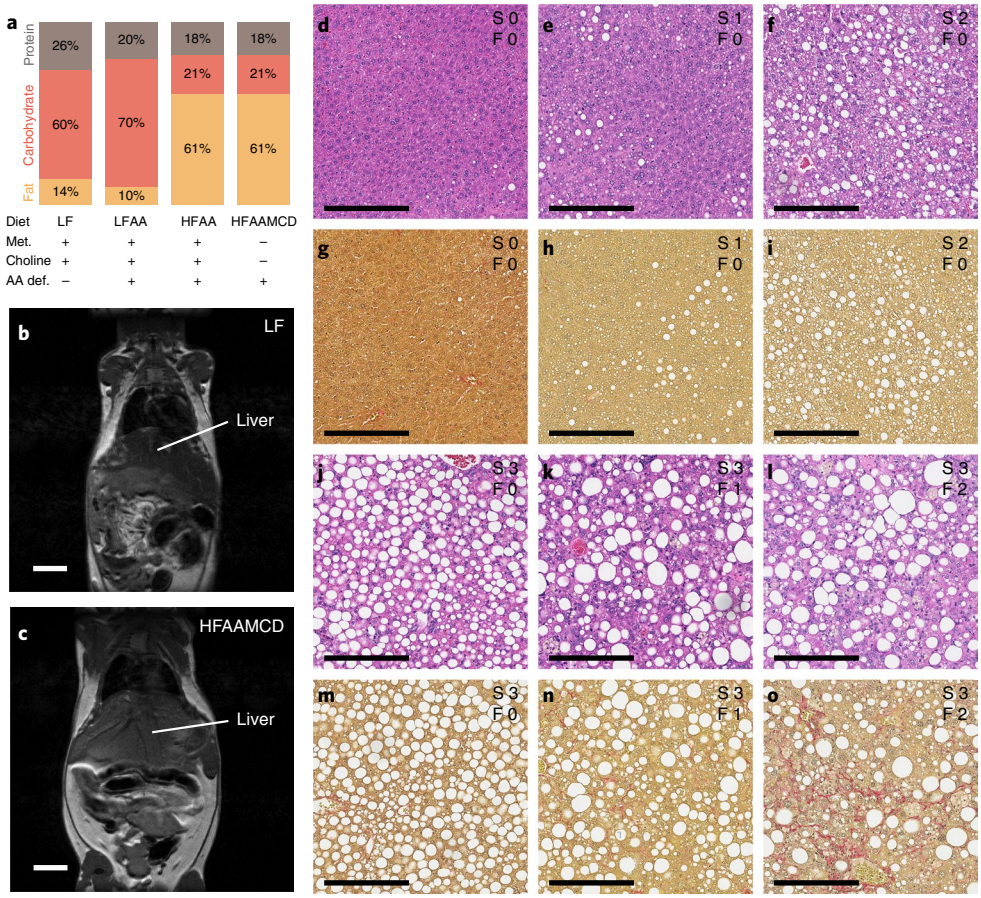

Fig. 2 | A diet-induced model of NAFLD/NASH leads to progressive steatosis followed by fibrosis in mouse livers. a, Diet composition, amino acid source, and methionine (Met.) and choline content were varied across the following four distinct diets: LF, LFAA, HFAA and HFAAMCD. The colours correspond to macromolecules in each diet: fat (orange), carbohydrate (red) and protein (brown). The plus sign indicates the presence of the corresponding feature; the minus sign indicates the absence of the corresponding feature. AA def., amino acid defined. **b**,**c**, T1-weighted MRI of the abdomen in mice—which were fed on an LF (**b**) or HFAAMCD (**c**) diet for 22 weeks—oriented along the coronal plane indicates liver steatosis and hepatomegaly. For **b** and **c**, scale bars, 6 mm. **d**–**o**, H&E (**d**–**f** and **j**–**l**) and Sirius Red (**g**–**i** and **m**–**o**) histology images of mouse livers (×20 magnification). Images of representative steatosis (S) grades 0 (**d** and **g**), 1 (**e** and **h**), 2 (**f** and **i**) and 3 (**j**–**o**) and fibrosis (F) grades 0 (**d**–**j** and **m**), 1 (**k** and **n**) and 2 (**l** and **o**) are shown. For **d**–**o**, scale bars, 200 μm.

Carr–Purcell–Meiboom–Gill (CPMG) pulse sequence to perform multicomponent T2 relaxometry. The samples were placed directly adjacent to the RF transceiver coil and fully spanned the sensitive region of the sensor (Fig. 1b).

The acquired signal was processed to infer a quantitative metric of fat content. The MR signals can be decomposed using a multiexponential model to identify constituent relaxation times and their corresponding amplitudes (Fig. 1c). The amplitude attributed to a particular relaxation time is a direct measure of the composition of the sample. The time-domain relaxometry signals show an increase in relaxation time with increasing fat fraction (Fig. 1d). These synthetic tissue phantoms and liver tissue produce multicomponent T2 decay signals due to the presence of multiple distinct water compartments (for example, intracellular versus extracellular)[30,31].

The slowest relaxation component corresponds to the fat compartment in these synthetic tissue phantoms[29]. The amplitude attributed to the fat compartment from the portable MR sensor measurements was directly related to the phantom fat fraction, as expected[27] (Fig. 1e). Similar results were acquired when phantoms were measured using a benchtop nuclear magnetic resonance (NMR) spectrometer, which serves as a gold standard for T2 relaxometry measurement (Supplementary Fig. 4). The benchtop NMR spectrometer could not be used as a viable clinical diagnostic tool owing to its small closed bore design and limited portability. Furthermore, this fitting procedure is able to robustly estimate amplitudes of distinct tissue compartments across a range of heterogenous tissue samples. We performed Monte-Carlo simulations to establish the necessary signal-to-noise ratio (SNR) for accurate tissue amplitude estimation (Supplementary Fig. 5). These findings show that this sensor can quantify the fat fraction using multicomponent T2 relaxometry.

A diet-induced mouse model of NAFLD and NASH induces a range of liver steatosis and fibrosis. We sought to induce liver steatosis and fibrosis within a mouse model of NAFLD and NASH progression. High-fat and nutrient-deficient diet-induced mouse models faithfully reproduce relevant pathophysiology observed in human disease, including progressive microvesicular and macrovesicular steatosis, and periportal and perisinusoidal fibrosis[32,33]. Mice were randomly assigned to one out of four diets: low fat (LF), a standard chow with no nutrient deficiency; low-fat amino acid defined (LFAA); high-fat amino acid defined (HFAA); and high-fat amino acid defined methionine and choline deficient (HFAAMCD)[34,35]. The high-fat diets (HFAA and HFAAMCD) contained 61% calories from fat, whereas the low-fat diets (LF and LFAA) contained between 14% and 10% calories from fat, respectively (Fig. 2a).

The HFAAMCD diet contained no choline and an approximately sixfold reduction in methionine compared with the normal levels (Fig. 2a and Supplementary Table 1). Mice were fed on these diets for between 1 and 40 weeks to observe a wide range of liver steatosis and fibrosis. The mice on the HFAAMCD diet exhibited marked and progressive hepatomegaly compared with mice that were fed the LF, LFAA and HFAA diets (Supplementary Fig. 6).

We established progression of steatosis using T1-weighted MRI of the mouse abdomen oriented along the coronal plane before (Fig. 2b) and after 22 weeks (Fig. 2c) of feeding on the HFAAMCD diet. Hepatomegaly and hyperintensity of the liver indicate steatohepatitis[36,37].

Haematoxylin and eosin (H&E) and Sirius Red (SR) histology slides were prepared from each liver and were together graded for steatosis and fibrosis on the basis of well-established guidelines[38]. Representative histology images across steatosis and fibrosis grades are shown in Fig. 2d–o. Severe steatosis developed rapidly with fibrosis following more gradually in the mice on the HFAAMCD diet (Supplementary Fig. 7). Mild steatosis developed consistently in the mice on the HFAA and LFAA diets. No steatosis or fibrosis was observed in the mice on the LF diet. Steatosis was exclusively microvesicular in cases of mild (grade 1) steatosis. Both macrovesicular and microvesicular steatosis was present in all cases of moderate (grade 2) and severe (grade 3) steatosis. Mild to moderate inflammation was present in most cases of severe steatosis, especially those with any fibrosis.

The portable MR sensor accurately predicts steatosis and fibrosis grade in ex vivo mouse livers. We next characterized the ability of the portable MR sensor to measure liver steatosis and fibrosis in a controlled setting without other confounding tissues (for example, intra-abdominal fat). Freshly excised livers from mice were scanned with the portable MR sensor using a CPMG pulse sequence (Fig. 3a).

Representative time-domain signals across steatosis grades show increased relaxation time with increased histological steatosis grade (Fig. 3b). The slowest relaxation component in a triexponential fit corresponds to the fat within the liver tissue, similar to the synthetic tissue phantoms. The fat amplitude estimated by the portable MR sensor is significantly different between steatosis grades and increases with increasing steatosis grade (Fig. 3c). Receiver operating characteristic (ROC) curves of classifiers between steatosis grades on the basis of the fat amplitude show a very strong ability to discriminate between grades (Fig. 3d). A confusion matrix showing the relationship between predicted and true steatosis grade shows high-accuracy performance across all steatosis grades (Fig. 3e). We validated the ability of multicomponent T2 relaxometry to accurately and reproducibly predict steatosis grade independently from our portable MR sensor using a benchtop NMR spectrometer (Supplementary Fig. 8).

We measured the fibrosis within livers using a DW measurement of fluid within the tissue. It is known that fibrosis is negatively associated with the diffusivity of water within livers[39]. Single-sided MR systems have previously demonstrated sensitivity to changes in sample diffusion[40–43]. Here we leverage the inherent field inhomogeneity of the static magnetic field to encode diffusivity by varying the echo time of the CPMG measurement. An increased echo time causes the signal to attenuate more rapidly in highly diffusive samples. Our portable MR sensor has the ability to estimate relative differences in sample diffusivity using DW multicomponent T2 relaxometry that are in agreement with gold-standard estimates, which were generated with a benchtop NMR spectrometer using pulse gradient spin echo measurements (Supplementary Fig. 9). Healthy liver exhibits a high self-diffusion coefficient of extracellular water compared with fibrotic livers[39,44]. Multicomponent T2 relaxometry enables identification of the signal attributed to each of the fluid compartments within the liver, that is, intracellular water, extracellular water and fat[30,31]. We define a DW liver signal as the difference in the amplitude of the extracellular fluid component at a short (65 μs) and long (520 μs) echo time.

This DW liver signal is correlated with fibrosis and is significantly different between fibrosis grades (Fig. 3f). ROC curves of classifiers between fibrosis grades on the basis of the DW liver signal show a strong ability to discriminate between grades (Fig. 3g). A confusion matrix showing the relationship between predicted and true fibrosis grade shows a high-accuracy performance across all fibrosis grades (Fig. 3h). These findings highlight the ability of our MR sensor to identify steatosis and fibrosis in mouse liver tissue, opening up the possibility of staging and tracking progression of NAFLD and NASH.

The portable MR sensor accurately quantifies the fat fraction in human liver. Our approach generalizes to human liver tissue obtained from whole ex vivo livers. We performed portable MR measurements on a piece of liver tissue and then performed H&E histological analysis on the same sample to grade steatosis. Fibrosis was not assessed, because an insufficient number of fibrotic livers were encountered during the study period. Representative H&E histology images across steatosis grades are shown in Fig. 4a–c. Steatosis was almost exclusively microvesicular in cases of mild (grade 1) steatosis. Both macrovesicular and microvesicular steatosis was present in all cases of moderate (grade 2) steatosis. Mild to moderate inflammation was present in some cases of mild steatosis and all cases of moderate steatosis.

Human liver tissue was placed on top of the sensor, and measurements were performed to identify liver steatosis (Fig. 4d). Representative time-domain signals across steatosis grades show an increased relaxation time in livers from patients with increased steatosis grade (Fig. 4e). The fat amplitude estimated by the portable MR sensor is significantly different between steatosis grades (Fig. 4f). ROC curves of classifiers between steatosis grades on the basis of the fat amplitude show a very strong ability to discriminate between grades (Fig. 4g). A confusion matrix showing the

Fig. 3 | The portable MR sensor accurately stages steatosis and fibrosis using multicomponent T2 relaxometry analysis of excised livers. a, Illustration of portable MR sensor measurements of excised mouse livers. **b**, Representative time-domain plots of the T2 decay curve from liver tissue for each steatosis grade. **c**, Estimated fat amplitude versus steatosis grade. The black lines indicate the median values. $***P<0.001$, $**P<0.01$, $*P<0.05$; NS, not significant. Statistical analysis was performed using one-way analysis of variance (ANOVA) between groups, with the Tukey–Kramer test for post hoc multiple comparisons ($P=1.2\times10^{-32}$, $F=174.02$). From left to right, $n=26$, $n=10$, $n=13$ and $n=26$ biologically independent mice. **d**, The ROC curves of classifiers between steatosis grades demonstrate an area under ROC (AUROC) of 0.99 (95% CI = 0.98–1.00; grade 0 versus 1–3), 1.00 (95% CI = 0.99–1.00; grade 0–1 versus 2–3) and 1.00 (95% CI = 0.98–1.00; grade 0–2 versus 3). **e**, A confusion matrix of predicted versus true steatosis demonstrates an overall accuracy of 92% and a Cohen's κ of 0.89 (95% CI = 0.80–0.97). **f**, Estimated DW liver signal (fibrosis) versus fibrosis grade. The black lines indicate the median values. $***P<0.001$, $**P<0.01$, $*P<0.05$. Statistical analysis was performed using one-way ANOVA between groups, with the Tukey–Kramer test for post hoc multiple comparisons ($P=2.6\times10^{-7}$; $F=37.41$). From left to right, $n=4$, $n=9$ and $n=9$ biologically independent mice. **g**, The ROC curves of classifiers between fibrosis grades demonstrate an AUROC of 1.00 (95% CI = 1.00–1.00; grade 0 versus 1–2) and 0.90 (95% CI = 0.79–0.96; grade 0–1 versus 2). **h**, A confusion matrix of predicted versus true fibrosis demonstrates an overall accuracy of 86% and a Cohen's κ of 0.78 (95% CI = 0.56–1.00).

relationship between predicted and true steatosis grade shows a high-accuracy performance across all steatosis grades (Fig. 4h). These findings show that our portable MR sensor can be used to accurately identify liver steatosis grade in human liver tissue samples using the same methods that were developed for liver steatosis in mice. Straightforward extensions of this approach could enable measurements of larger liver tissue samples for both ex vivo and in vivo use.

Spatially selective differential acquisition enables highly localized remote measurements. A non-invasive measurement of the liver in vivo requires that the sensor has the ability to measure

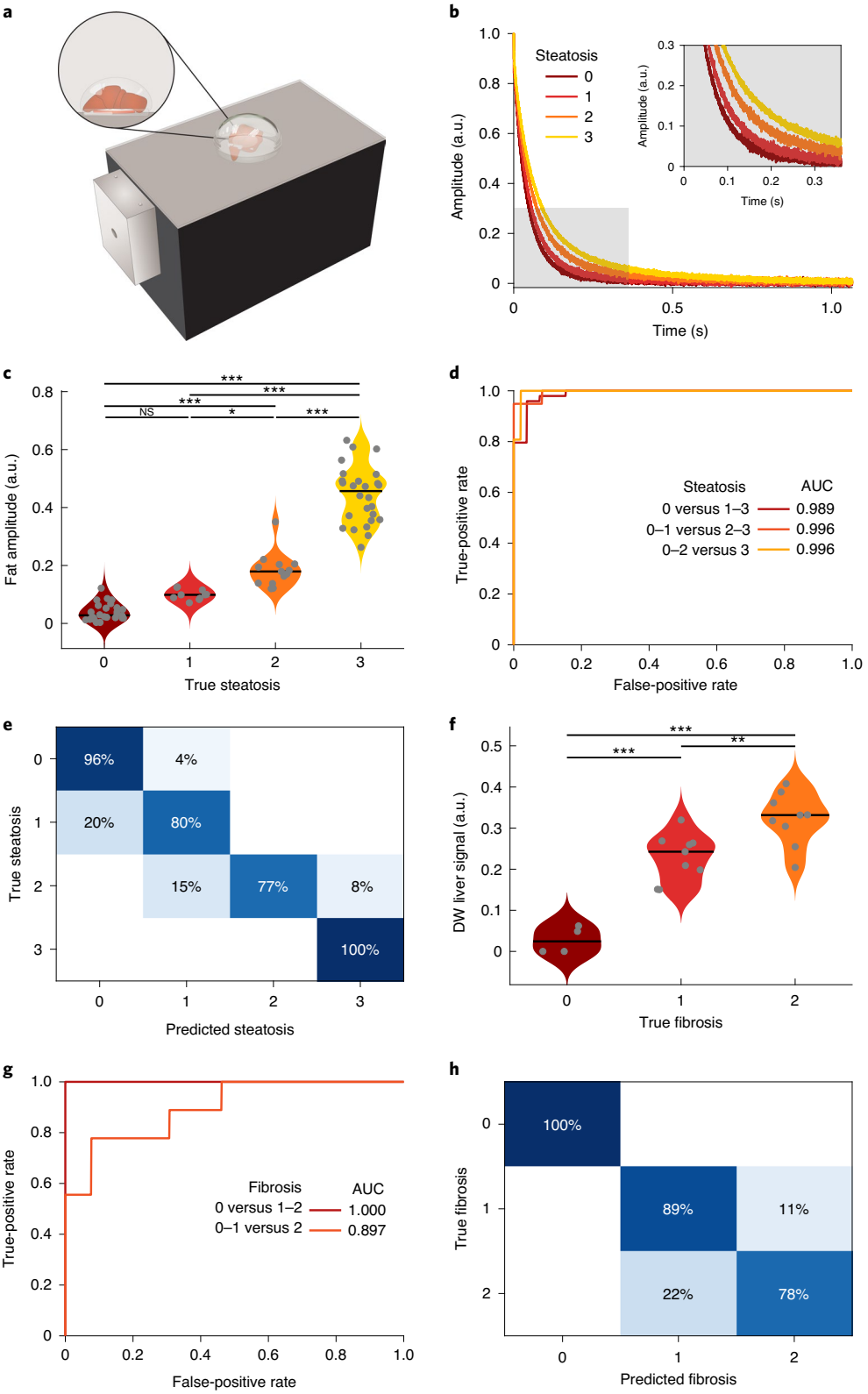

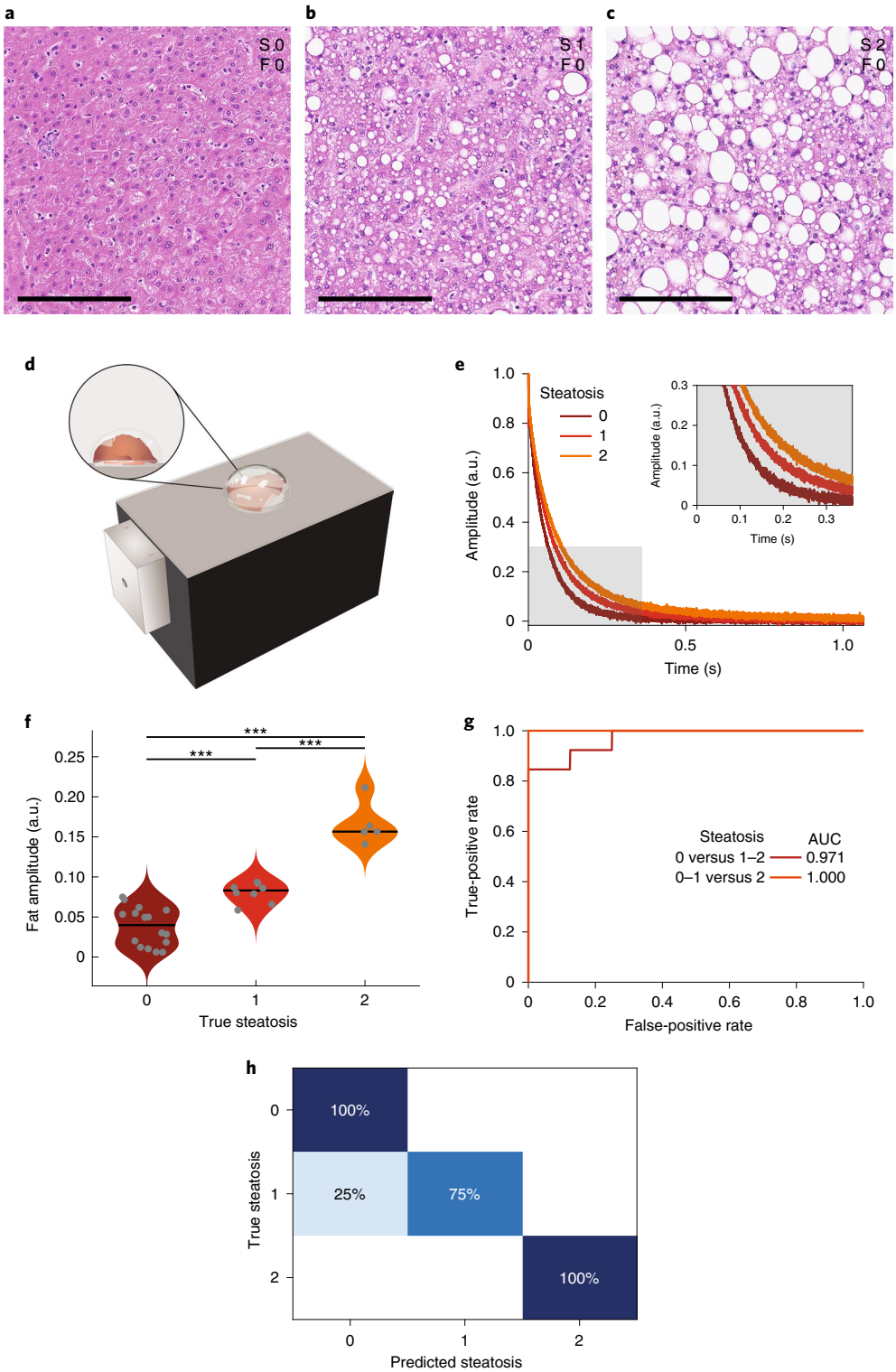

Fig. 4 | The portable MR sensor accurately stages steatosis from excised human livers. a–c, H&E histology images of human livers (×20 magnification). Images of representative steatosis (S) grades 0 (**a**), 1 (**b**) and 2 (**c**). Scale bars, 200 µm. **d**, Illustration of portable MR sensor measurements of excised tissue samples from human livers. **e**, Representative time-domain plots of the T2 decay curve from liver tissue for each steatosis grade. **f**, Estimated fat amplitude versus steatosis grade. The black lines indicate the median values. $^{***}P < 0.001$. Statistical analysis was performed using one-way ANOVA between groups, with the Tukey–Kramer test for post hoc multiple comparisons ($P = 7.3 \times 10^{-11}$; $F = 65.29$). From left to right, $n = 16$, $n = 8$ and $n = 5$ independent samples. **g**, The ROC curves of classifiers between steatosis grades demonstrate an AUROC of 0.97 (95% CI = 0.90–0.99; grade 0 versus 1–2) and 1.00 (95% CI = 1.00–1.00; grade 0–1 versus 2). **h**, A confusion matrix of predicted versus true steatosis demonstrates an overall accuracy of 93% and a Cohen's κ of 0.88 (95% CI = 0.72–1.00).

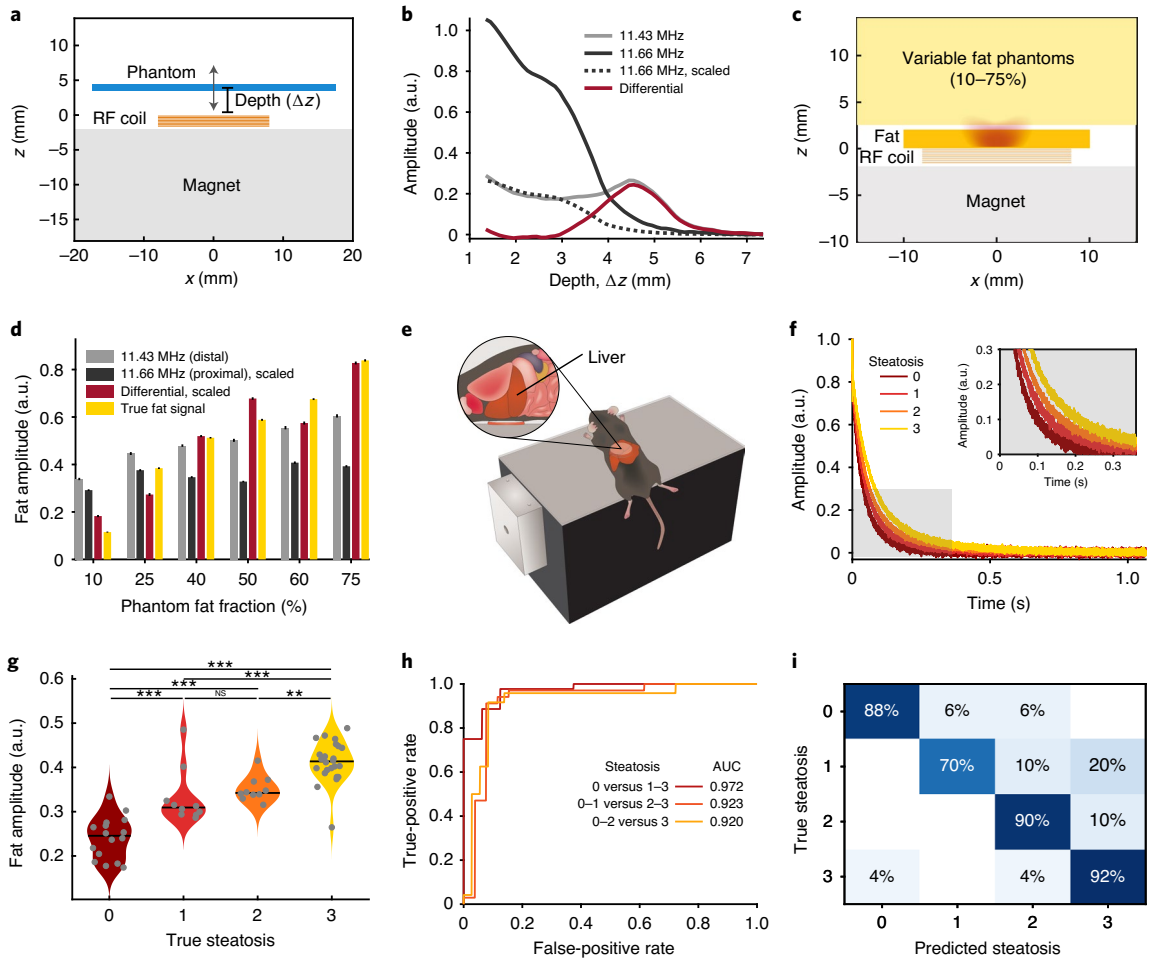

Fig. 5 | The portable MR sensor accurately stages steatosis in vivo using multicomponent T2 relaxometry. a, Illustration of the depth profiling experiment, indicating scanning of a planar sample along the depth (Δz) axis above the sensor. **b**, Acquired depth profiles at 11.43 MHz (light grey) and 11.66 MHz (dark grey) RF excitation frequency; and a scaled depth profile at 11.66 MHz (dark grey, dotted). A differential (red) depth profile was derived as the weighted difference between the two acquired depth profiles. **c**, Illustration of the depth-resolved fat phantom experiment with proximal (constant fat fraction) and distal (varied fat fraction) synthetic tissue layers. **d**, Estimated fat amplitude with portable MR sensor with an RF excitation frequency of 11.43 MHz (distal, light grey) and 11.66 MHz (proximal, dark grey); the differential estimate (red) derived as the weighted difference of the two acquired estimates; and the true fat signal estimate when measuring the phantom only with no proximal spacer (yellow). **e**, Illustration of in vivo, non-invasive liver measurement using a portable MR sensor. **f**, Representative time-domain plots of the T2 decay curve from liver tissue for each steatosis grade. **g**, Estimated fat amplitude versus steatosis grade. The black lines indicate the median values. $^{***}P < 0.001$, $^{**}P < 0.01$; $^{*}P < 0.05$. Statistical analysis was performed using one-way ANOVA between groups, with the Tukey–Kramer test for post hoc multiple comparisons ($P = 2.5 \times 10^{-14}$; $F = 41.91$). From left to right, $n = 16$, $n = 10$, $n = 10$ and $n = 24$ biologically independent mice. **h**, ROC curves of the classifiers between steatosis grades demonstrate an AUROC of 0.97 (95% CI = 1.00–0.92; grade 0 versus 1–3), 0.92 (95% CI = 0.81–0.98; grade 0–1 versus 2–3) and 0.92 (95% CI = 0.82–0.97; grade 0–2 versus 3). **i**, A confusion matrix of predicted versus true steatosis demonstrates an overall accuracy of 87% and a Cohen's κ of 0.81 (95% CI = 0.69–0.93).

tissue located within the mouse abdomen. The ideal system would avoid more-proximal tissues that may confound the measurement, such as skin and subcutaneous tissue. The static magnetic field strength is highly uniform in the direction parallel to the surface of the sensor while decreasing gradually when moving away from its surface (Supplementary Fig. 10). We characterized the sensitivity of the system as a function of depth at two excitation frequencies, which were used to encode spatial information. A thin planar phantom was scanned along a line perpendicular to the surface of the sensor and repeatedly measured at each excitation frequency (Fig. 5a). These results were validated by an independent characterization of sensitivity as a function of depth at twelve unique RF excitation frequencies, demonstrating depth selectivity and a trade-off between depth and signal strength (Supplementary Fig. 11).

We designed an acquisition strategy to localize our measurement to a mouse liver in vivo. The sensor is more sensitive to samples located at a distance of 1–4 mm when operated at 11.66 MHz and 1–6 mm at 11.43 MHz (Fig. 5b, dark and light grey, solid). A measurement at 11.43 MHz would provide some sensitivity to a mouse liver, but the measurement would be confounded by more-proximal tissues owing to the non-zero magnitude of the 11.43 MHz signal in a region 1–3 mm from the sensor surface. We therefore sought to design an acquisition strategy to localize the measurement solely to a region distal (approximately 3–6 mm) from the surface of the sensor. We computed the optimal scaling factor that, when applied to the 11.66 MHz sensitivity profile, best aligned its most proximal region (0–3 mm) to that of the 11.43 MHz signal (Fig. 5b, dark grey, dotted). We then uniformly scaled the time-domain signal generated from an 11.66 MHz signal with this scaling factor.

We designed our system to compute the difference between this scaled time-domain signal and the signal acquired at 11.43 MHz to generate a differential signal that provides highly localized sensitivity to a region solely distal from the surface of the sensor (Fig. 5b, red).

We constructed a proximal synthetic tissue phantom with a constant fat fraction (50%) and a distal phantom with variable fat fractions (10–75% fat; Fig. 5c) to demonstrate the use of this approach. Measurements performed at 11.66 MHz, with a mean penetration depth of 3 mm, were unable to identify changes in the fat fraction of the more-distal phantom (Fig. 5d, dark grey). Measurements performed at 11.43 MHz, with a mean penetration depth of 5 mm, identified these changes, but failed to accurately represent the wide range of fat fractions, as is evident by the small range of measured fat amplitudes (Fig. 5d, light grey). By contrast, the differential measurement was able to both identify changes in fat fraction and more faithfully capture the wide range of fat fractions that were observed in the distal phantom (Fig. 5d, red). Moreover, the differential measurement most closely matches estimates of fat amplitude with the same portable MR sensor with no proximal fat spacer present (Fig. 5d, yellow). This shows that our system can perform highly localized measurements of tissue remote from the surface of the sensor while minimizing confounding signal from more-proximal tissue. This approach avoids the use of more traditional, complex gradient coils for spatial encoding, enabling the sensor to remain simple and low-cost.

The portable MR sensor accurately quantifies steatosis in vivo. We then applied this measurement strategy to identify liver steatosis within anaesthetized mice that were placed on top of our sensor (Fig. 5e). Scans were performed over a 10 min period in free breathing animals. Representative time-domain signals across steatosis grades show an increased relaxation time with increased steatosis grade (Fig. 5f). The fat amplitude estimated by the portable MR sensor is significantly different between steatosis grades (Fig. 5g). ROC curves of classifiers between steatosis grades on the basis of the fat amplitude show a very strong ability to discriminate between grades (Fig. 5h). A confusion matrix showing the relationship between predicted and true steatosis grade shows a high-accuracy performance across all steatosis grades (Fig. 5i). We did not assess the ability of our sensor to identify fibrosis grade in vivo owing to animal welfare restrictions on total anaesthesia time. These findings show that our portable MR sensor can identify liver steatosis grade in vivo.

We hypothesized that, when our system overestimated steatosis grade, the signal may have been confounded by subcutaneous and/or intra-abdominal fat. Of the six mice whose steatosis grade was overestimated, 50% had a body weight in the top tenth percentile (Supplementary Fig. 12). Furthermore, the predicted fat amplitude was strongly correlated between ex vivo and in vivo measurements with the portable MR sensor, with the exception of mice with the highest body weight and, therefore, the greatest amount of visceral fat (Supplementary Fig. 13). This suggests that our measurement inadvertently attributed excess subcutaneous and/or intra-abdominal fat with more severe liver steatosis. We developed a technique that first estimates proximal tissue (for example, subcutaneous and/or intra-abdominal fat) thickness and then performs a scan at a sufficient depth such that the majority of the signal originates from the more-distal tissue (for example, liver) to overcome variations in proximal confounding tissue (Supplementary Fig. 14). The presence of proximal confounding tissue demonstrates the value of an improved sensor for use in humans. Acquisition in free-breathing animals may have introduced intra-animal variability or reduced SNR due to the respiratory cycle and thoracic movement. We performed numerical simulations of additional magnet arrays for single-sided MR sensors, which indicated that the straightforward modifications to the sensor design described here can extend the penetration depth (Supplementary Fig. 15). Further improvements to signal localization and acquisition would ultimately allow for a prospective clinical trial investigating the diagnostic and prognostic utility of a portable MR sensor.

Discussion

An ideal diagnostic biomarker for NAFLD and NASH would be highly specific and sensitive, low cost, non-invasive, automated and portable to enable longitudinal monitoring of disease progression. Here we demonstrated a portable MR system that has the ability to (1) accurately identify liver steatosis and fibrosis in excised mouse liver, (2) localize its measurement to a distal region to avoid more-proximal confounding tissues and (3) accurately identify liver steatosis within mice in vivo and within human liver tissue. A portable MR sensor may have the ability to improve the screening of at-risk individuals, enable longitudinal tracking of disease progression to guide clinical interventions and help in the development of new therapeutics.

Traditional MRI has demonstrated highly accurate quantification and liver steatosis and fibrosis. However, MRI is unsuitable for routine use owing to its high cost, long measurement time, and requirements for dedicated operators and facilities[22–24]. Our MR sensor offers the potential to leverage the versatility of MRI within a portable (7 kg), compact, low-power-consumption technology. The device is straightforward to deploy and requires no skilled operator for data acquisition or measurement interpretation, therefore eliminating the cost associated with the interpretation of MRI data performed by a radiologist. A cost-effectiveness analysis found that a low-cost MR-based technique would be superior to liver biopsy[45].

A major advantage of a portable MR sensor is its ability to efficiently sample a large volume of liver in a single measurement. Liver biopsy core samples represent only around 1/50,000th of the total liver volume, which introduces sampling variation. Sampling bias is especially relevant in NAFLD, in which substantial heterogeneity has been reported[46]. Liver biopsies are associated with pain, organ injury, bleeding and death[47–51]. Patient attrition is high in investigational studies that require regular liver biopsies, which precludes longitudinal sampling[52]. An imaging-based approach, such as the one described here, has the potential to sample the entire liver volume, overcoming the most substantial limitation of liver biopsy (that is, spatial sampling bias) as well as patient discomfort, injury and bleeding.

Our measurement directly examines the accumulation of fat and progression of fibrosis. Although blood sampling is relatively non-invasive and offers a convenient method for repeated assessment of liver function, it measures liver-specific markers. Liver-specific markers (such as alanine aminotransferase, aspartate aminotransferase, alkaline phosphatase, gamma glutamyl transpeptidase and bilirubin) offer neither a highly specific nor sensitive method for identifying NAFLD onset or progression[53,54]. Direct measurement of steatosis and fibrosis offers a potentially more accurate estimate of disease onset and progression. Our approach is potentially complementary to MRE as it offers an estimate of fibrosis on the basis of microstructural changes in water compartmentalization, whereas MRE focuses on macroscopic changes in tissue stiffness. Further applications of this approach could enable diagnosis and longitudinal tracking of liver tumours and hepatic iron overload.

Mouse models of liver steatosis and fibrosis for NAFLD and NASH that are induced by high-fat and nutrient-deficient diets are ubiquitous and well accepted. These models faithfully reproduce relevant pathophysiology observed in human disease, including progressive microvesicular and macrovesicular steatosis, and periportal and perisinusoidal fibrosis[33]. Furthermore, these models induce increased expression of genes that are associated with lipogenesis, inflammatory cytokines, oxidative stress and serum

liver enzyme activity[33,55]. In this study, we were unable to independently assess hepatocellular ballooning and lobular inflammation, which are key hallmarks of NAFLD and NASH progression, as their presence was highly correlated with that of steatosis in this mouse model.

A portable MR sensor can also have considerable diagnostic utility for surgeons who perform liver transplants or hepatic resection. Moderate and severe steatosis (for example, >30% macrosteatosis) are independent risk factors during liver transplantation for significant morbidity, including the risk of immediate non-function, the need for renal replacement therapy, early allograft dysfunction and decreased patient survival[56–58]. Current methods for screening for liver steatosis, particularly in cases of donation after circulatory death, are subjective and inaccurate, leading to excessive liver discards, further exacerbating the organ shortage[59]. A non-invasive measure of liver steatosis would enable widespread screening of candidate livers before transplantation to enable informed selection of deceased donors as well as improved screening of living donors. Furthermore, an objective measure of steatosis would assist with preoperative preparation for hepatic liver resection. Patients with hepatic steatosis undergoing partial hepatectomy have significantly higher postoperative morbidity compared with those without steatosis, which is attributable to severe ischaemia–reperfusion injury during resection and impaired parenchymal regeneration thereafter[60]. There is a clear need for prompt, point-of-care assessment of liver steatosis to enable transplant surgeons to make objective decisions about organ utilization.

A non-invasive MR device with the ability to isolate its measurement to liver tissue would require a localization technique that performs well across heterogeneous patients. Our in vivo measurements of liver steatosis may have been confounded by more-proximal fat located in the intraperitoneal or subcutaneous space, especially in mice with higher body weight. Improvements to the geometrical design of the sensor would improve the spatial selectivity of the measurement. Previously described portable MR sensors have demonstrated penetration depths of several centimetres, suggesting a potential development path[61,62]. Efforts to increase the penetration depth of our device to enable a robust in vivo measurement of human liver tissue would probably increase the mass of the device and, therefore, partially compromise portability compared with the sensor described here. Our previous experience testing a portable MR sensor in a hospital setting shows that a device mounted onto a cart provides a suitable form-factor for point-of-care diagnostics[63]. Despite these modest increases in sensor mass, the cost and portability would remain substantially improved compared with clinical MRI, and this would result in improved access to diagnostic tests performed with this sensor in both hospital and outpatient settings. The primary challenge is achieving an optimal balance between penetration depth, magnetic-field strength and sensor portability. New approaches to designing single-sided sensors, such as incorporating concepts from other single-sided sensors, may be necessary to achieve penetration depths of several centimetres without excessively compromising portability[61,62]. The pulse sequences and signal processing techniques described here are expected to generalize to single-sided sensors designed using alternative approaches beyond the Unilateral Linear Halbach array. More sophisticated acquisition strategies could be implemented through new pulse-sequence design to efficiently map the relevant anatomy and isolate the signal originating from the liver. Future efforts to design a portable MR sensor for clinical use must find the most appropriate trade-off between accessibility, versatility across patient populations and diagnostic utility.

Validation of this technology would require a prospectively designed clinical study in a representative patient population. It would then be possible to consider how this measurement, together with existing clinical risk-factors, performs as a diagnostic or prognostic of NAFLD and NASH, rather than comparing it solely against histological grading.

In summary, this research introduces the concept of portable MR sensors as a point-of-care diagnostic tool for staging liver steatosis and fibrosis. Broad availability of low-cost staging and monitoring for disease progression from NAFLD to NASH would enable earlier diagnosis, more-accurate patient stratification and more-straightforward evaluation of investigational therapies.

Methods

Study design. The objective of the study was to determine whether multicomponent T2 relaxometry localized to the liver using a portable MR sensor could identify and accurately stage steatosis and fibrosis for use as a diagnostic of NAFLD and NASH. We first demonstrated accurate fat fraction quantification with synthetic tissue phantoms using this approach. We then showed that liver steatosis and fibrosis can be measured using our portable MR sensor by leveraging differences in compartmental T2 relaxation rate and diffusivity. We finally applied this technique to grade steatosis in mice as well as in human liver samples. MR feature extraction and analysis methods were prospectively determined. Sample sizes were determined using power calculations on the basis of effect sizes that were estimated from pilot experiments. No outliers were excluded from data analysis. Investigators were blinded to the identity of mice during measurement, data analysis and pathology grading.

Mouse model. The animal studies were approved by the Massachusetts Institute of Technology Institutional Animal Care and Use Committee (0716-045-19) and animals were cared for at the US Department of Agriculture-inspected MIT Animal Facility under federal, state, local and National Institutes of Health guidelines for animal care. Male C57BL/6NCrl mice (aged 6–7 weeks) were purchased from Charles River Laboratories. The mice were provided ad libitum access to standard chow for at least 72 h before the start of experiments to allow for acclimation. Distinct cohorts of mice were placed on one of the following diets for one to forty weeks: L-amino acid defined high-fat (60% kcal fat) diet with 0.1% methionine and no added choline (HFAAMCD, Research Diets A06071302); L-amino acid defined high-fat (60% kcal fat) diet with normal methionine and choline (HFAA, Research Diets A06071306); L-amino acid defined low-fat (10% kcal fat) diet with normal methionine and choline (LFAA, Research Diets A06071314); and standard chow (14% fat; LF, LabDiet Prolab Isopro RMH 3000 5P76). The average in vivo MR signal acquisition time was approximately 10 min (240 averages), and in vivo acquisition did not include respiratory gating. Animals were anaesthetized using an IMPAC6 anaesthesia system (VetEquip, 901808) equipped with isoflurane (Patterson Veterinary, 07-893-1389) at a flow rate of 0.5 l min^{-1}.

Discarded human liver model. Human donor livers that were declined for transplantation by all of the transplant centres in the donation service area between May and August 2019, with consent for research, were included in this study. All of the donor livers were received through New England Donor Services (NEDS); no organs were procured from prisoners. Donors or their surrogates (including parents or legal guardians) provided informed consent for use of donor organs in research. The Massachusetts General Hospital Institutional Review Board (IRB) and the NEDS previously approved the use of discarded human tissue (2011P001496), and all studies were performed in accordance with IRB and NEDS approved guidelines. All of the donor livers were procured using the standard technique of in situ cold flush using University of Wisconsin preservation solution and transported using conventional static cold storage[64]. Multiple wedge liver biopsies were taken from each liver for MR analysis in conjunction with machine perfusion experiments[65].

Histology and pathology. Liver samples (mouse, rat and human) were fixed in 10% neutral buffered formalin for 24 h, stored in 70% ethanol, processed to paraffin and embedded. The samples were sectioned at a thickness of 5 µm and stained with either H&E or SR at the MIT Koch Institute Histology Core Facility. Images were acquired using a Leica Aperio AT2 slide scanner at ×20 magnification.

Steatosis was graded on a scale of 0 to 3 by evaluating parenchymal involvement at low to medium magnification power (0 for <5% involvement; 1 for 5–33%, 2 for 34–66%; and 3 for >66%)[38]. Fibrosis was graded using SR slides on a scale of 0 to 4 (0 for none; 1 for perisinusoidal or periportal; 2 for perisinusoidal and portal/periportal; 3 for bridging fibrosis; and 4 for cirrhosis). All grading was performed by a pathologist who was blinded to the identity of each mouse.

Multiexponential fitting. CPMG T2 decay curves were modelled as multiexponential signals to extract relaxation times (τ_i) and relative amplitudes (A_i). Echo integrals were computed as the sum of the points sampled for each echo during CPMG when more than one point was collected for each echo. A general multicomponent exponential decay signal was represented as:

$$\hat{y}(t, \mathbf{A}, \boldsymbol{\tau}) = \sum_{i=1}^{N} A_i \times \exp(-t/\tau_i) \quad (1)$$

where $\hat{y}(t)$ is the estimated signal, N is the number of components, $\mathbf{A}$ is a vector of amplitudes and $\boldsymbol{\tau}$ is a vector of corresponding relaxation times. Two models were used to represent the multicomponent nature of these signals in this study. The first optimizes over both the relaxation times and relative amplitudes. The optimal set of parameters is found by minimizing the L2-norm of the residuals between the estimated and the measured signal:

$$\mathbf{A}^{\text{opt}}, \boldsymbol{\tau}^{\text{opt}} = \underset{\mathbf{A},\boldsymbol{\tau}}{\text{argmin}} \|y(t) - \hat{y}(t)\|_2 \quad (2)$$

where $y(t)$ is the measured signal and $\|\cdot\|_2$ represents the L2-norm. This model enables the discovery of the relaxation times and amplitudes of a multiexponential signal. The second model optimizes only over the amplitudes, because the relaxation times are specified as parameters:

$$\mathbf{A}^{\text{opt}} = \underset{\mathbf{A}}{\text{argmin}} \|y(t) - \hat{y}(t, \boldsymbol{\tau})\|_2 \quad (3)$$

This more constrained model enables the amplitudes to be estimated more accurately and differences between signals to be described solely as amplitude changes. SNR was defined as the maximum magnitude value divided by the s.d. of the noise. The noise distribution was estimated from the residuals of the fit.

Fabrication of the fat fraction phantom. Fat fraction phantoms were fabricated, as previously described[27]. The components of the aqueous phase were deionized water, sodium benzoate, Tween-20 and agar (Sigma-Aldrich). The components of the fat phase were peanut oil and SPAN 80 (Sigma-Aldrich).

Portable MR sensor design and construction. The portable MR sensor, which was designed and constructed in house, consists of a permanent magnet array and an RF transceiver coil. The magnet array within the sensor comprises 180 individual N52 (Nd1Fe14B) cube magnets with a side length of 0.5 inch (12.7 mm). The magnets are arranged in a three-dimensional grid with 6×6×5 magnets in the x, y and z directions, respectively. The spacing between the magnets is 2.23, 0.76 and 2.54 mm in the x, y and z directions, respectively. The magnets located in the second, third and fourth slices along the z direction are oriented with their positive pole facing the positive z direction. The magnets located in the first and fifth slices along the z direction are oriented with their positive pole facing the negative and positive y direction, respectively. The magnets located in the third slice along the z direction are offset by 5.1 mm in the negative y direction. The magnets are housed within an aluminium housing manufactured with a dimensional tolerance of 0.127 mm. An RF transceiver coil was located on top of the magnet and consisted of an eight-turn solenoid (AWG 32, wire diameter, 202 µm) wound around a cylindrical PTFE bobbin (diameter, 16 mm). The coil geometry was selected to maximize the sensitivity of the sensor. We tested several tightly wound solenoid coils varying in diameter and number of turns were tested, and selected the coil that maximized the SNR on a large sample intended to span the entire sensitive region of the sensor. The magnets were enclosed within an aluminium housing for mechanical stability and electric grounding. A Kea2 spectrometer (Magritek) generated the CPMG pulse sequence for MR measurements and was connected to the transceiver coil through a two-element L impedance matching circuit.

Portable MR sensor characterization. The profile of the static magnetic field of the portable MR sensor was characterized by scanning a Hall probe (HMMT-6J04-VR, Lake Shore Cryotronics) connected to a gaussmeter (Model 475 DSP Gaussmeter) along lines corresponding to the z axis and y axis and centred with respect to the top surface of the sensor.

The measurement of initial sensitivity profiles versus depth was performed by scanning a thin, planar sample of aqueous $CuSO_4$ along a line perpendicular to the sensor surface. The sample consisted of a 1 mm × 16 mm × 32 mm pocket machined into a polyether ether ketone (PEEK) holder filled with aqueous $CuSO_4$. PEEK was used as it produced a negligible MR signal. Measurements were performed with the centre of the sample located between 1.35 mm and 7.35 mm from the sensor surface. The surface of the sensor was defined as the top of the RF coil (as opposed to the surface of the magnet).

The measurement of subsequent sensitivity profiles versus depth was performed by scanning a thin planar sample that was oriented parallel to the surface of the sensor along a line perpendicular to its surface. The sample consisted of a 380 µm × 6 mm × 6 mm pocket machined into PEEK stock filled with an aqueous solution of $CuSO_4$. Measurements were performed with the centre of the sample located between 0.690 mm and 6.59 mm from the surface of the sensor.

Measurements were performed with the CPMG pulse sequence with 2,000 echoes, 65 µs echo time, 110 ms repetition time, 1 µs dwell time (1 MHz acquisition bandwidth), 12 µs pulse duration and 16 acquired points per echo using a Kea2 spectrometer (Magritek).

Portable MR sensor measurements and post-processing. T2 measurements were performed with the portable MR sensor using a CPMG pulse sequence. The sample under study for each experiment was placed in direct contact with the sensor and aligned with the sensitive region (that is, directly adjacent to the RF transceiver coil). A plastic cap covering the liver during scanning was used to minimize the effect of evaporation on the tissue structure. A Kea2 spectrometer (Magritek) was responsible for pulse-sequence generation. The average in vivo MR signal acquisition time was 10 min, and in vivo acquisition did not include respiratory gating. Measurements were performed in an unshielded environment without using a Faraday cage. All data acquired with the portable MR sensor were modelled as a multicomponent exponential decay (equation (1)) and fit to the model that is described in equation (2). The resulting time constants, corresponding to distinct compartments, were learned from the fit result and were subsequently used in equation (3) to quantify relative signal amplitude originating from each compartment.

MRI image acquisition. MRI scans were acquired using a 7R/310/ASR (Agilent, formerly Varian) scanner with vnmrj (v.3.2b) equipped with a 38 mm whole-body coil. Qualitative T1-weighted scans were performed with fast spin echo multi slice with a 256×256 resolution, 143 ms repetition time and 20 ms echo time. Image reconstruction was performed using the standard built-in method provided by vnmrj.

Statistical analysis. Differences between groups were assessed using ANOVA with Tukey–Kramer test for post hoc multiple comparisons. The 95% CIs ($\alpha = 0.05$) for all of the parameter estimates, shown with error bars, in multicomponent exponential fits were computed assuming an asymptotic normal distribution for each estimate.

Reporting summary. Further information on research design is available in the Nature Research Reporting Summary linked to this article.

Data availability

The main data supporting the results in this study are available within the paper and its Supplementary Information. The raw and analysed datasets generated during the study are too large to be publicly shared, yet they are available for research purposes from the corresponding author on reasonable request.

Code availability

All code used for the analysis of data generated during the study is available from the corresponding author on reasonable request.

Received: 25 November 2019; Accepted: 28 September 2020;
Published online: 30 November 2020

References

1. Younossi, Z. et al. Global burden of NAFLD and NASH: trends, predictions, risk factors and prevention. *Nat. Rev. Gastroenterol. Hepatol.* **15**, 11–20 (2018).
2. Shetty, A. & Syn, W.-K. Health and economic burden of nonalcoholic fatty liver disease in the United States and its impact on veterans. *Fed. Pract.* **36**, 14–19 (2019).
3. Spengler, E. K. & Loomba, R. Recommendations for diagnosis, referral for liver biopsy, and treatment of nonalcoholic fatty liver disease and nonalcoholic steatohepatitis. *Mayo Clin. Proc.* **90**, 1233–1246 (2015).
4. Brunt, E. M. Pathology of nonalcoholic fatty liver disease. *Nat. Rev. Gastroenterol. Hepatol.* **7**, 195–203 (2010).
5. Vernon, G., Baranova, A. & Younossi, Z. M. Systematic review: the epidemiology and natural history of non-alcoholic fatty liver disease and non-alcoholic steatohepatitis in adults. *Aliment. Pharmacol. Ther.* **34**, 274–285 (2011).
6. Takahashi, Y. & Fukusato, T. Histopathology of nonalcoholic fatty liver disease/nonalcoholic steatohepatitis. *World J. Gastroenterol.* **20**, 15539–15548 (2014).
7. Wattacheril, J., Issa, D. & Sanyal, A. Nonalcoholic steatohepatitis (NASH) and hepatic fibrosis: emerging therapies. *Annu. Rev. Pharmacol. Toxicol.* **58**, 649–662 (2018).
8. Zhang, E. et al. Cost-utility analysis of nonalcoholic steatohepatitis screening. *Eur. Radiol.* **25**, 3282–3294 (2015).
9. Tanaka, N. et al. Current status, problems, and perspectives of non-alcoholic fatty liver disease research. *World J. Gastroenterol.* **25**, 163–177 (2019).
10. Wong, V. W.-S., Adams, L. A., de Lédinghen, V., Wong, G. L.-H. & Sookoian, S. Noninvasive biomarkers in NAFLD and NASH—current progress and future promise. *Nat. Rev. Gastroenterol. Hepatol.* **15**, 461–478 (2018).
11. Strauss, S., Gavish, E., Gottlieb, P. & Katsnelson, L. Interobserver and intraobserver variability in the sonographic assessment of fatty liver. *Am. J. Roentgenol.* **189**, W320–W323 (2007).

12. Liang, W. et al. Establishment of a general NAFLD scoring system for rodent models and comparison to human liver pathology. *PLoS ONE* **9**, e115922 (2014).
13. Shen, J. et al. Non-invasive diagnosis of non-alcoholic steatohepatitis by combined serum biomarkers. *J. Hepatol.* **56**, 1363–1370 (2012).
14. Krawczyk, K. et al. Adipohormones as prognostic markers in patients with nonalcoholic steatohepatitis (NASH). *J. Physiol. Pharmacol.* **60**, 71–75 (2009).
15. Loomba, R. et al. Magnetic resonance elastography predicts advanced fibrosis in patients with nonalcoholic fatty liver disease: a prospective study. *Hepatology* **60**, 1920–1928 (2014).
16. Akkaya, H. E., Erden, A., Öz, D. K., Ünal, S. & Erden, I. Magnetic resonance elastography: basic principles, technique, and clinical applications in the liver. *Diagn. Interv. Radiol.* **24**, 328–335 (2018).
17. Fishbein, M. et al. Hepatic MRI for fat quantitation: its relationship to fat morphology, diagnosis, and ultrasound. *J. Clin. Gastroenterol.* **39**, 619–625 (2005).
18. Taouli, B. et al. Diffusion-weighted MRI for quantification of liver fibrosis: preliminary experience. *Am. J. Roentgenol.* **189**, 799–806 (2007).
19. Petitclerc, L., Sebastiani, G., Gilbert, G., Cloutier, G. & Tang, A. Liver fibrosis: review of current imaging and MRI quantification techniques. *J. Magn. Reson. Imaging* **45**, 1276–1295 (2017).
20. Dulai, P. S., Sirlin, C. B. & Loomba, R. MRI and MRE for non-invasive quantitative assessment of hepatic steatosis and fibrosis in NAFLD and NASH: clinical trials to clinical practice. *J. Hepatol.* **65**, 1006–1016 (2016).
21. Bohte, A. E., van Werven, J. R., Bipat, S. & Stoker, J. The diagnostic accuracy of US, CT, MRI and ^{1}H-MRS for the evaluation of hepatic steatosis compared with liver biopsy: a meta-analysis. *Eur. Radiol.* **21**, 87–97 (2011).
22. Schultz, J. F., Bell, J. D., Goldstein, R. M., Kuhn, J. A. & McCarty, T. M. Hepatic tumor imaging using iron oxide MRI: comparison with computed tomography, clinical impact, and cost analysis. *Ann. Surg. Oncol.* **6**, 691–698 (1999).
23. Evens, R. G. & Evens, R. G. Economic and utilization analysis of MR imaging units in the United States in 1987. *Radiology* **166**, 27–30 (1988).
24. Schroeder, S. A. Magnetic resonance imaging: present costs and potential gains. *Ann. Intern. Med.* **102**, 551–553 (1985).
25. Bashyam, A., Frangieh, C., Li, M. & Cima, M. J. Dehydration assessment via a non-invasive, miniature, portable magnetic resonance sensor using multicomponent T2 relaxometry. *Magn. Reson. Med.* **83**, 1390–1404 (2020).
26. Bashyam, A., Li, M. & Cima, M. J. Design and experimental validation of unilateral linear Halbach magnet arrays for single-sided magnetic resonance. *J. Magn. Reson.* **292**, 36–43 (2018).
27. Bush, E. C. et al. Fat-water phantoms for magnetic resonance imaging validation: a flexible and scalable protocol. *J. Vis. Exp.* **139**, e57704 (2018).
28. Hines, C. D. G. et al. T1 independent, T2* corrected MRI with accurate spectral modeling for quantification of fat: validation in a fat-water-SPIO phantom. *J. Magn. Reson. Imaging* **30**, 1215–1222 (2009).
29. Bernard, C. P., Liney, G. P., Manton, D. J., Turnbull, L. W. & Langton, C. M. Comparison of fat quantification methods: a phantom study at 3.0T. *J. Magn. Reson. Imaging* **27**, 192–197 (2008).
30. Whitaker, C. & Casarella, J. Multiple NMR T2 relaxation values in human liver tissue. *Am. J. Roentgenol.* **141**, 1203–1208 (1983).
31. Cole, W. C., Leblanc, A. D. & Jhingran, S. G. The origin of biexponential T2 relaxation in muscle water. *Magn. Reson. Med.* **29**, 19–24 (1993).
32. Clapper, J. R. et al. Diet-induced mouse model of fatty liver disease and nonalcoholic steatohepatitis reflecting clinical disease progression and methods of assessment. *Am. J. Physiol. Gastrointest. Liver Physiol.* **305**, G483–G495 (2013).
33. Nakamura, A. & Terauchi, Y. Lessons from mouse models of high-fat diet-induced NAFLD. *Int. J. Mol. Sci.* **14**, 21240–21257 (2013).
34. Matsumoto, M. et al. An improved mouse model that rapidly develops fibrosis in non-alcoholic steatohepatitis. *Int. J. Exp. Pathol.* **94**, 93–103 (2013).
35. Ikawa-Yoshida, A. et al. Hepatocellular carcinoma in a mouse model fed a choline-deficient, l-amino acid-defined, high-fat diet. *Int. J. Exp. Pathol.* **98**, 221–233 (2017).
36. van Werven, J. R. et al. Assessment of hepatic steatosis in patients undergoing liver resection: comparison of US, CT, T1-weighted dual-echo MR imaging, and point-resolved ^{1}H MR spectroscopy. *Radiology* **256**, 159–168 (2010).
37. Charlton, M. et al. Fast food diet mouse: novel small animal model of NASH with ballooning, progressive fibrosis, and high physiological fidelity to the human condition. *Am. J. Physiol. Gastrointest. Liver Physiol.* **301**, G825–G834 (2011).
38. Kleiner, D. E. et al. Design and validation of a histological scoring system for nonalcoholic fatty liver disease. *Hepatology* **41**, 1313–1321 (2005).
39. Bonekamp, S., Torbenson, M. S. & Kamel, I. R. Diffusion-weighted magnetic resonance imaging for the staging of liver fibrosis. *J. Clin. Gastroenterol.* **45**, 885–892 (2011).
40. Casanova, F., Perlo, J. & Blümich, B. *Single-Sided NMR* (Springer, 2011).
41. Casieri, C., Bubici, S. & De Luca, F. Self-diffusion coefficient by single-sided NMR. *J. Magn. Reson.* **162**, 348–355 (2003).
42. Rata, D. G., Casanova, F., Perlo, J., Demco, D. E. & Blümich, B. Self-diffusion measurements by a mobile single-sided NMR sensor with improved magnetic field gradient. *J. Magn. Reson.* **180**, 229–235 (2006).
43. Perlo, J., Casanova, F. & Blümich, B. Profiles with microscopic resolution by single-sided NMR. *J. Magn. Reson.* **176**, 64–70 (2005).
44. Koinuma, M., Ohashi, I., Hanafusa, K. & Shibuya, H. Apparent diffusion coefficient measurements with diffusion-weighted magnetic resonance imaging for evaluation of hepatic fibrosis. *J. Magn. Reson. Imaging* **22**, 80–85 (2005).
45. Eddowes, P. J. et al. Utility and cost evaluation of multiparametric magnetic resonance imaging for the assessment of non-alcoholic fatty liver disease. *Aliment. Pharmacol. Ther.* **47**, 631–644 (2018).
46. Skoien, R. et al. Heterogeneity of fibrosis patterns in non-alcoholic fatty liver disease supports the presence of multiple fibrogenic pathways. *Liver Int.* **33**, 624–632 (2013).
47. Howlett, D. C., Drinkwater, K. J., Lawrence, D., Barter, S. & Nicholson, T. Findings of the UK national audit evaluating image-guided or image-assisted liver biopsy. Part II. Minor and major complications and procedure-related mortality. *Radiology* **266**, 226–235 (2013).
48. Castéra, L., Nègre, I., Samii, K. & Buffet, C. Patient-administered nitrous oxide/oxygen inhalation provides safe and effective analgesia for percutaneous liver biopsy: a randomized placebo-controlled trial. *Am. J. Gastroenterol.* **96**, 1553–1557 (2001).
49. Piccinino, F. et al. Complications following percutaneous liver biopsy: a multicentre retrospective study on 68,276 biopsies. *J. Hepatol.* **2**, 165–173 (1986).
50. Seeff, L. B. et al. Complication rate of percutaneous liver biopsies among persons with advanced chronic liver disease in the HALT-C trial. *Clin. Gastroenterol. Hepatol.* **8**, 877–883 (2010).
51. Rockey, D. C., Caldwell, S. H., Goodman, Z. D., Nelson, R. C. & Smith, A. D. Liver biopsy. *Hepatology* **49**, 1017–1044 (2009).
52. Foster, G. R. et al. Management of chronic hepatitis C: clinical audit of biopsy based management algorithm. *Brit. Med. J.* **315**, 453–458 (1997).
53. Clark, J. M., Brancati, F. L. & Diehl, A. M. Nonalcoholic fatty liver disease. *Gastroenterology* **122**, 1649–1657 (2002).
54. Yano, E., Tagawa, K., Yamaoka, K. & Mori, M. Test validity of periodic liver function tests in a population of Japanese male bank employees. *J. Clin. Epidemiol.* **54**, 945–951 (2001).
55. Stanković, M. N. et al. Time-dependent changes and association between liver free fatty acids, serum lipid profile and histological features in mice model of nonalcoholic fatty liver disease. *Arch. Med. Res.* **45**, 116–124 (2014).
56. Linares, I., Hamar, M., Selzner, N. & Selzner, M. Steatosis in liver transplantation: current limitations and future strategies. *Transplantation* **103**, 78–90 (2019).
57. Croome, K. P. et al. The impact of post-reperfusion syndrome during liver transplantation using livers with significant macrosteatosis. *Am. J. Transplant.* https://doi.org/10.1111/ajt.15330 (2019).
58. Gabrielli, M. et al. Steatotic livers. Can we use them in OLTX? Outcome data from a prospective baseline liver biopsy study. *Ann. Hepatol.* **11**, 891–898 (2012).
59. Croome, K. P., Lee, D. D. & Taner, C. B. The "skinny" on assessment and utilization of steatotic liver grafts: a systematic review. *Liver Transpl.* **25**, 488–499 (2019).
60. Selzner, M. & Clavien, P. A. Fatty liver in liver transplantation and surgery. *Semin. Liver Dis.* **21**, 105–113 (2001).
61. Rehorn, C. & Blümich, B. Cultural heritage studies with mobile NMR. *Angew. Chem. Int. Ed. Engl.* **57**, 7304–7312 (2018).
62. Dabaghyan, M. et al. A portable single-sided magnet system for remote NMR measurements of pulmonary function. *NMR Biomed.* **27**, 1479–1489 (2014).
63. Colucci, L. A. et al. Fluid assessment in dialysis patients by point-of-care magnetic relaxometry. *Sci. Transl. Med.* **11**, eaau1749 (2019).
64. Bruinsma, B. G. et al. Subnormothermic machine perfusion for ex vivo preservation and recovery of the human liver for transplantation. *Am. J. Transplant.* **14**, 1400–1409 (2014).
65. Karimian, N. et al. Ex situ normothermic machine perfusion of donor livers. *J. Vis. Exp.* **2015**, e52688 (2015).

Acknowledgements

We thank staff at the Koch Institute Swanson Biotechnology Center for technical support, specifically W. Huang and V. Spanoudaki at Animal Imaging and Preclinical Testing and K. Cormier at Histology; A. Warren, K. Nayak, M. Rosen, E. Adalsteinsson, S. Carrasco, K. Subramanyam, M. Cotler, E. Rousseau and K. Ramadi for discussions; staff at the New England Donor Services and the patients and families that made this study possible. This work was supported in part by the Koch Institute Support (core) grant no. P30-CA14051 from the National Cancer Institute, the National Institutes of Health grant nos. R01DK096075 and R01DK107875, and National Science Foundation (ATP-Bio 1941543). A.B. was supported by a Fannie & John Hertz Foundation Graduate Fellowship and a National Science Foundation Graduate Fellowship.

Author contributions

A.B. constructed the portable MR sensor. A.B. and C.J.F. characterized the portable MR sensor, performed all of the experiments and wrote the manuscript. J.S. performed ex vivo experiments. A.B. prepared figures. A.B., C.J.F. and M.J.C. designed the experiments and interpreted results. A.B., C.J.F., S.R. and M.J.C. edited the manuscript. R.T.B. conducted pathology analysis of all tissues. M.J.C., D.A.A., H.Y. and K.U. supervised the research.

Competing interests

A.B. and M.J.C. are inventors on a patent application (US20180306879) submitted by MIT that describes the design of the permanent magnet array within the portable MR sensor. K.U. has a financial interest in Organ Solutions, a company that is focused on developing organ preservation technology. These interests are managed by the Mass General Brigham in accordance with their conflict of interest policies.

Additional information

Supplementary information is available for this paper at https://doi.org/10.1038/s41551-020-00638-0.

Correspondence and requests for materials should be addressed to M.J.C.

Reprints and permissions information is available at www.nature.com/reprints.

Publisher's note Springer Nature remains neutral with regard to jurisdictional claims in published maps and institutional affiliations.

nature research

Corresponding author(s): Michael Cima

Last updated by author(s): Sep 14, 2020

Reporting Summary

Nature Research wishes to improve the reproducibility of the work that we publish. This form provides structure for consistency and transparency in reporting. For further information on Nature Research policies, see our Editorial Policies and the Editorial Policy Checklist.

Statistics

For all statistical analyses, confirm that the following items are present in the figure legend, table legend, main text, or Methods section.

n/a	Confirmed	
☐	☒	The exact sample size (*n*) for each experimental group/condition, given as a discrete number and unit of measurement
☐	☒	A statement on whether measurements were taken from distinct samples or whether the same sample was measured repeatedly
☐	☒	The statistical test(s) used AND whether they are one- or two-sided *Only common tests should be described solely by name; describe more complex techniques in the Methods section.*
☒	☐	A description of all covariates tested
☐	☒	A description of any assumptions or corrections, such as tests of normality and adjustment for multiple comparisons
☐	☒	A full description of the statistical parameters including central tendency (e.g. means) or other basic estimates (e.g. regression coefficient) AND variation (e.g. standard deviation) or associated estimates of uncertainty (e.g. confidence intervals)
☐	☒	For null hypothesis testing, the test statistic (e.g. *F*, *t*, *r*) with confidence intervals, effect sizes, degrees of freedom and *P* value noted *Give P values as exact values whenever suitable.*
☒	☐	For Bayesian analysis, information on the choice of priors and Markov chain Monte Carlo settings
☒	☐	For hierarchical and complex designs, identification of the appropriate level for tests and full reporting of outcomes
☐	☒	Estimates of effect sizes (e.g. Cohen's *d*, Pearson's *r*), indicating how they were calculated

Our web collection on statistics for biologists contains articles on many of the points above.

Software and code

Policy information about availability of computer code

Data collection	Benchtop NMR data were collected with Bruker minispec commercial software. MRI data were collected with vnmrj software (version 3.2b) (commercial). Portable MR data were collected with Magritek Prospa (v3.50) commercial software.
Data analysis	MestReNova v12.0.4, Graphpad Prism 8 and MATLAB v2018b were used to perform all data analyses and statistics. Built-in (commercial) packages were used for these operations.

For manuscripts utilizing custom algorithms or software that are central to the research but not yet described in published literature, software must be made available to editors and reviewers. We strongly encourage code deposition in a community repository (e.g. GitHub). See the Nature Research guidelines for submitting code & software for further information.

Data

Policy information about availability of data

All manuscripts must include a data availability statement. This statement should provide the following information, where applicable:

- Accession codes, unique identifiers, or web links for publicly available datasets
- A list of figures that have associated raw data
- A description of any restrictions on data availability

The main data supporting the results in this study are available within the paper and its Supplementary Information. The raw and analysed datasets generated during the study are too large to be publicly shared, yet they are available for research purposes from the corresponding author on reasonable request.

Field-specific reporting

Please select the one below that is the best fit for your research. If you are not sure, read the appropriate sections before making your selection.

☒ Life sciences ☐ Behavioural & social sciences ☐ Ecological, evolutionary & environmental sciences

For a reference copy of the document with all sections, see nature.com/documents/nr-reporting-summary-flat.pdf

Life sciences study design

All studies must disclose on these points even when the disclosure is negative.

Sample size	Sample sizes were determined with power calculations based on effect sizes estimated from pilot experiments.
Data exclusions	No outliers were excluded from data analyses as part of a pre-specified analysis plan.
Replication	A replication cohort of mice were used to validate the findings after the initial results had been obtained. All attempts at replication were successful.
Randomization	Mice were randomly assigned to experimental groups (diet and duration of diet).
Blinding	The investigators were blinded to the identification of mice during measurements, data analysis and pathology grading.

Reporting for specific materials, systems and methods

We require information from authors about some types of materials, experimental systems and methods used in many studies. Here, indicate whether each material, system or method listed is relevant to your study. If you are not sure if a list item applies to your research, read the appropriate section before selecting a response.

Materials & experimental systems

n/a	Involved in the study
☒	☐ Antibodies
☒	☐ Eukaryotic cell lines
☒	☐ Palaeontology and archaeology
☐	☒ Animals and other organisms
☐	☒ Human research participants
☒	☐ Clinical data
☒	☐ Dual use research of concern

Methods

n/a	Involved in the study
☒	☐ ChIP-seq
☒	☐ Flow cytometry
☒	☐ MRI-based neuroimaging

Animals and other organisms

Policy information about studies involving animals; ARRIVE guidelines recommended for reporting animal research

Laboratory animals	Male C57BL/6NCrl mice were purchased from Charles River Laboratories at 6–7 weeks of age. Weight was not recorded upon receipt.
Wild animals	The study did not involve wide animals.
Field-collected samples	The study did nov involve samples collected from the field.
Ethics oversight	The animal studies were approved by the Massachusetts Institute of Technology Institutional Animal Care and Use Committee (0716-045-19). The animals were cared for in the U.S. Department of Agriculture–inspected MIT Animal Facility under federal, state, local, and National Institutes of Health guidelines for animal care.

Note that full information on the approval of the study protocol must also be provided in the manuscript.

Human research participants

Policy information about studies involving human research participants

Population characteristics	Patients who were declared brain-dead in the New England area with consent for organ donation and research were included in this study if the donated liver was rejected for transplantation by all transplant centers in the New England region and subsequently offered for research use. In this particular study, biopsies of the livers were taken for analysis. This portion of the study is limited by the nature of the organ donation process, since these organs are an extremely scarce resource for research. Organ donors can vary greatly in demographic characteristics as a result, although the focus of this study is limited

	to the presence of steatosis and fibrosis in the liver biopsies. Age ranged from 46 to 63, and a mix of both male and female donors were included.
Recruitment	Patients in the New England Donor Service Area who were declared brain-dead and had provided consent for organ donation were subsequently consented for providing organs for research by the donation coordinators of the New England Donor Services (the Organ Procurement Organization in the New England Donor Service Area). During organ retrieval, donor livers that were rejected for transplantation by all transplant centers in the New England region were subsequently offered to the Organ Preservation Laboratory at Massachusetts General Hospital for research. These donated livers are classified as 'discarded human tissue' and provided as part of a long-standing collaboration between the MGH Organ Preservation Lab and the New England Donor Services. As such, the study investigators were not involved in the consent process and did not obtain consent or interact with the organ donors or their proxies.
Ethics oversight	Massachusetts General Hospital Institutional Review Board, New England Donor Services

Note that full information on the approval of the study protocol must also be provided in the manuscript.